communications physics

Article

https://doi.org/10.1038/s42005-024-01737-z

Quantized polarization and Majorana fermions beyond tenfold classification

Check for updates

Sang-Hoon Han[1,3], Myungjun Kang[1,3], Moon Jip Park[1] ✉ & Sangmo Cheon[1,2] ✉

Exploration of topology is central in condensed matter physics and applications to fault-tolerant quantum information. The bulk-boundary correspondence and tenfold classification determine the topological state compared to a vacuum. Contrary to this belief, we demonstrate that topological zero-energy domain-wall states can emerge for all forbidden 1D classes of the tenfold classification table. The guiding principle is that the difference in the topological quantities of two trivial domains can be quantized, and hence, a topologically protected state can emerge at the domain wall. Such nontrivial domain-wall states are demonstrated using generalized Su-Schrieffeer-Heeger and generalized Kitaev models, which manifest quantized polarization and Majorana fermions, respectively. The quantized Berry phase difference between the domains protects the non-trivial nature of the domain-wall states, extending the bulk-boundary correspondence, also confirmed by the tight-binding and Jackiw-Rebbi methods. Furthermore, we show that the seemingly trivial electronic and superconducting models can be transformed into their topological counterparts in the framework of the topological Fermi-liquid theory. Finally, we propose potential systems where our results may be realized, spanning from electronic and superconducting to optical systems.

The tenfold classification of the topological periodic table provides a systematic understanding of topological insulators and superconductors using time-reversal (T), particle–hole (C), and chiral (Γ) symmetries (Fig. 1a)[1,2]. As a guiding principle of topological materials, the bulk-boundary correspondence[3,4] predicts robust topological boundary states against perturbation, which has potential applications in many subfields of physics, including spintronics[5,6], ultracold atomic gases[7,8], photonics[9,10], and mechanics[11,12]. In particular, topological superconductors and their boundary modes (or Majorana fermions) are expected to open novel quantum computation technology with the help of quantum braiding[13,14]. Furthermore, new types of topological phases have been discovered using finer topological classifications in topological crystalline insulators and superconductors, where a crystalline point group symmetry protects topological boundary states[15,16]. Similarly, higher-order topological phases[17] and topological semimetal phases are also classified[18,19]. Beyond the conventional classifications, several studies have tried to find a method that still results in topological phases; for example, sub-symmetry-protected topological phases and quasi-symmetry-protected topological semimetal were investigated[20,21]. These classifications lead to robust topological phases as well as unexpected topology beyond the usual space group classifications, even in the absence of full symmetry. As an alternative guiding principle, our endeavors are focused on revealing whether topological zero-energy states can exist for the systems of topologically trivial classes, as shown in Fig. 1a because such an extension will open a new pathway for robust topological applications and technology.

Usually, a topological phase of a bulk is determined by the existence of topological states at the edges and a nontrivial topological number by comparing them with a vacuum (or an atomic limit), and the topological number is calculated considering all the filled electronic/superconducting states in the band structure. However, it is recognized that topological quantities such as the Berry phase and Berry curvature depend on the band structure near the Fermi level, which is fully consistent with the Fermi-liquid theory in the viewpoint of a topological Fermi-liquid theory[22]. Here, even for a seemingly topologically trivial class, we show that the topological zero-energy states can emerge at the center of a domain wall when the difference of the topological quantities between the corresponding two domains is quantized and the low-energy effective theory is still topological from the perspective of topological Fermi-liquid theory. Thus, our findings diverge from the topological classification for defects[23], as defect classifications typically require that one of the domains remain topological.

In this work, we start our discussion by demonstrating the emergence of the topological zero-energy domain-wall state in 1D insulating chains using the generalized Su–Schrieffer–Heeger (SSH) models. In the original

[1]Department of Physics, Hanyang University, Seoul, 04763, South Korea. [2]Research Institute for Natural Science and High Pressure, Hanyang University, Seoul, 04763, South Korea. [3]These authors contributed equally: Sang-Hoon Han, Myungjun Kang. ✉e-mail: moonjippark@hanyang.ac.kr; sangmocheon@hanyang.ac.kr

(a)

d=1	T	C	Γ	Index
A	0	0	0	NA
AI	+	0	0	NA
AII	−	0	0	NA
AIII	0	0	1	ℤ
BDI	+	+	1	ℤ
C	0	−	0	NA
CI	+	−	1	NA
CII	−	−	1	ℤ
D	0	+	0	$\mathbb{Z}_2$
DIII	−	+	1	$\mathbb{Z}_2$

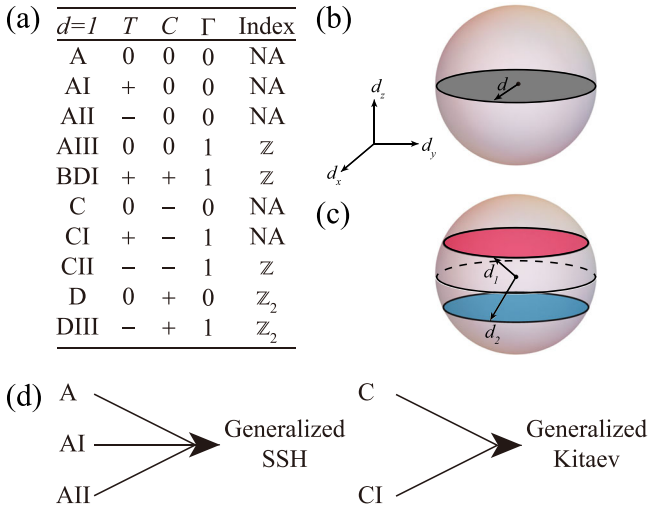

Fig. 1 | Classification table and schematics of the generalized Su–Schrieffer–Heeger (SSH) and Kitaev models. a Classification of the tenfold Altland-Zirnbauer classes in 1D. The lack of symmetry is presented with 0. For the antiunitary time-reversal (T) and particle–hole (C) symmetries, + and − distinguish the cases in which the symmetry operators' squares become I or $-I$. The absence and existence of chiral symmetry (Γ) is expressed via 0 and 1, respectively. $\mathbb{Z}$ and $\mathbb{Z}_2$ represent topological indices, while NA indicates topology is not allowed. **b**, **c** Schematics for the d vector distribution in the Bloch sphere for the generalized SSH models described by the 1D Dirac Hamiltonian in Eq. (1). In **b**, the d vector of the SSH model is constrained on the equator from chiral symmetry, and the solid angle surrounded by the d vector is 0 or 2π for the two degenerate groundstates. Therefore, the domain-wall state connecting the two groundstates has a quantized polarization. In **c**, the d vector of the generalized SSH model is not constrained in the Bloch sphere's equator; hence, neither groundstate has a quantized polarization. However, if the two degenerate groundstates have symmetrical d vectors (red and blue circles), the solid angle difference can be quantized as 2π, which can result in a quantized polarization for the corresponding domain-wall systems. **d** Schematics of the relation between the generalized SSH and Kitaev models and the classes where there is no topological index.

SSH model, which belongs to the BDI class, two energetically degenerate groundstates are topologically distinct and have quantized Berry phases[24,25] such as 0 and π depending on the solid angle swept by the so-called d vector in the corresponding Bloch sphere (Fig. 1b), where the d vector comes from the Dirac-type Bloch Hamiltonian $H(k) = \vec{d}(k) \cdot \vec{\sigma}$ with Pauli matrix σ_i. Therefore, the domain-wall configuration connecting two topologically distinct groundstates generates a topological zero-energy state with quantized electric polarization. Such a zero-energy state is known as the Jackiw–Rebbi zero-mode in the 1D relativistic quantum field theory[26,27]. Expanding the SSH model, we investigate a domain-wall configuration belonging to the AI class, where particle–hole and chiral symmetries are broken (Fig. 1a). While any one of the groundstates does not have a quantized Berry phase (Fig. 1c), the quantized difference of the Berry phase between the adjoined domains results in the zero-energy domain-wall state having quantized electric polarization. Furthermore, our seemingly trivial generalized SSH chain can be transformed into the topological SSH chain through unitary transformations from the perspective of the low-energy effective topological Fermi-liquid theory.

According to the modern theory of polarization and topological field theory, a domain wall state can possess the amount of polarization corresponding to the Berry phase difference between two domains[28,29]. However, whether the domain-wall configuration that has quantized Berry phase difference hosts a topological zero-energy state has not yet been studied. Moreover, such a concept has not been extended to the superconducting system because the corresponding topological zero-energy state, a Majorana fermion, should be described by the Majorana representation, which is the cumbersome split electron representation.

Therefore, we confirm the emergence of topological zero-energy domain-wall states for all 1D trivial electronic and superconducting classes using the generalized SSH and Kitaev models, as summarized in Fig. 1d. Consequently, such insulating and superconducting systems demonstrate quantized electric polarization and Majorana fermions, respectively.

Results and discussion

Extended bulk-boundary correspondence for electronic systems

We investigate the minimal tight-binding model belonging to the topologically trivial AI class as the representative insulating system using the generalized SSH model[30]. The tight-binding Hamiltonian is comprised of the Hamiltonian of the SSH model H_{SSH}[31] and the symmetry-breaking potential terms H_{on}[32], as shown in Fig. 2:

$$H_{\mathrm{AI}} = H_{\mathrm{SSH}} + H_{\mathrm{on}},$$
$$H_{\mathrm{SSH}} = \sum_n t_{n+1,n} c_{n+1}^{\dagger} c_n + h.c.,$$
$$H_{\mathrm{on}} = \sum_n m_z \left(c_{2n-1}^{\dagger} c_{2n-1} - c_{2n}^{\dagger} c_{2n} \right),$$

where $c_n^{\dagger}/c_n$ indicates the creation/annihilation operator for site $n = 1, \cdots, N$. The nearest-neighbor hopping parameter is $t_{n+1,n} = t_0 + (-1)^{n-1}\Delta/2$ with t_0 and Δ being the hopping amplitude and energy-valued dimerization, respectively. m_z is the strength of the onsite staggered potential. If m_z is constant, the Hamiltonian becomes that of the RM model[32]. The corresponding Dirac-type Bloch Hamiltonians obtained using conventions I and II are given as,

$$H_{\mathrm{AI}}^{(\mathrm{I})}(k) = \vec{d}(k) \cdot \vec{\sigma}, \tag{1}$$

$$H_{\mathrm{AI}}^{(\mathrm{II})}(k) = 2t_0 \cos(ka)\sigma_x - \Delta \sin(ka)\,\sigma_y + m_z\sigma_z, \tag{2}$$

where $d_x = (t_0 + \Delta/2) + (t_0 - \Delta/2)\cos(2ka)$, $d_y = (t_0 - \Delta/2)\sin(2ka)$, and $d_z = m_z$. The length of the unit cell is $2a$ and for simplicity, we set $a = 1$. See more information about the Bloch Hamiltonian convention in Supplementary Note 1.1. When $m_z = 0$, the Hamiltonian is simplified into the SSH model having time-reversal, particle–hole, and chiral symmetry, $\{H, \sigma_z\} = 0$[31]. However, for nonzero m_z, this Hamiltonian has time-reversal symmetry ($T = K$) but neither particle–hole nor chiral symmetry.

From the Bloch Hamiltonian, the energy eigenvalue is given by $E = \pm\sqrt{4t_0^2\cos^2 k + \Delta^2 \sin^2 k + m_z^2}$. In particular, Δ and m_z act as order parameters because they distinguish various groundstates, as shown in Fig. 2a. When $m_z = 0$, there exist energetically degenerate groundstates A and B. On the other hand, when $m_z \neq 0$, there exist four energetically degenerate groundstates (A', B', A'', B'') depending on the signs of Δ and m_z. If m_z is constant, the RM Hamiltonian has two degenerate groundstates, either A', B' or A'', B''.

We now consider three types of domain-wall configurations that connect the various groundstates [indicated by the red, blue, and green lines in Fig. 2a]. The schematic geometric configurations for the three types of domain-wall configurations are shown in Fig. 2b. In this case, Δ and m_z are no longer constants but become spatially varying functions connecting two groundstates. For instance, for the SSH (RM) domain-wall configurations, where the domain wall center is located at $x = 0$, the dimerization spatially varies in the form of $\Delta(x) = \Delta_0 \tanh(x/\xi_1)$ with $\Delta_0 < 0$ throughout the chain connecting A and B (A' and B') groundstates when $m_z = 0$ ($m_z = \mathrm{const.}$)[31,32]. When m_z is additionally interpolated, such as $m_z(x) = m_0 \tanh(x/\xi_2)$ with $m_0 < 0$, a new type of domain wall emerges connecting the A' and B'' groundstates, which is labeled as the AI domain-wall configuration or shortly, the AI chain. Here, ξ_i is the characteristic length scale of the domain wall.

The energy eigenvalues and wavefunction distributions of the finite chains corresponding to the three domain-wall configurations are shown in

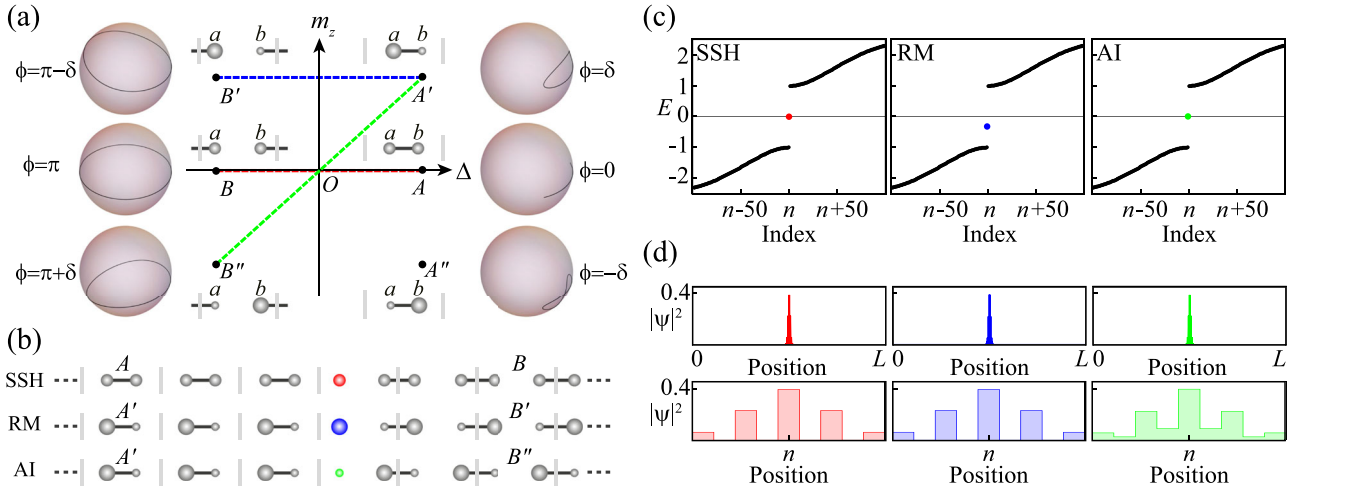

Fig. 2 | Generalized Su–Schrieffer–Heeger (SSH) chains. a Schematics for various groundstates and domain-wall configurations for the generalized SSH models in the order-parameter space comprised of energy-valued dimerization (Δ) and onsite energy m_z. Groundstates are labeled using capital letters (A, B, A', B', A'', B''), and the a and b in the unit cell represent two sublattice atoms. The black line in each Bloch sphere indicates the trajectory of the d vector for each groundstate, and ϕ indicates the value of the Berry phase, where δ is a positive number. The SSH, Rice–Mele (RM), and AI domain-wall configurations are represented by red, blue, and green dotted lines, respectively. **b** Schematics for the SSH (top), RM (middle), and AI (bottom) chains. The red, blue, and green spheres indicate the center of the corresponding 1D chains. **c** Energy eigenvalues of finite SSH, RM, and AI chains, of the corresponding ingap states. The points indicating the ingap states are magnified by two for clarity. The SSH and AI chains show topological zero-energy domain-wall states indicated by red and green. On the other hand, the RM chain shows topologically trivial non-zero-energy domain-wall states at $E = -m_z$ indicated by blue. **d** Total wavefunctions and their zoom-ins near the domain-wall states for the SSH, RM, and AI chains. For $n \pm 1$ and $n \pm 3$ sites of the zoom-ins, the data is magnified ten times. The hopping parameter is $t_0 = 1.2$ for all three cases with dimerization $\Delta(x)$ interpolated from 0.96 to −0.96 along the chain. The onsite energy m_z is fixed at 0.3 for the RM chain and interpolated from 0.3 to − 0.3 for the AI case. For all cases, the characteristic length is given by $\xi_1 = \xi_2 = 5$. For numerical calculation, $L = 2n - 1 = 249$ atoms are applied (with approximately $n = 125$ unit cells).

Fig. 2(c,d). The ingap state in the SSH (RM) chain is located at zero (non-zero) energy, and the corresponding wavefunctions of the ingap states are localized at the domain wall, as expected. Surprisingly, the AI chain exhibits the emergence of the zero-energy domain-wall state. Figure 2d shows zoom-ins of the wavefunction distributions near the domain wall, which exhibits a slight difference between the AI chain and the others. However, such a difference is not problematic but consistent with the analytical solution, which will be discussed later. In addition, to compare the domain-wall states with the usual edge states, we investigate the ingap states localized at the left and right edges for the same type of three chains systems but extended to have both left and right edge states (Fig. S3); due to chiral symmetry breaking, the RM and AI chains exhibit non-zero-energy edge states, while the SSH chain has topological zero-energy edge states.

When we consider the tight-binding Hamiltonian of a finite chain system, H_{AI}, we find that the SSH and AI chains satisfy the global chiral symmetry $\{H_{\mathrm{AI}}, \Gamma\} = 0$, which protects the zero-energy states localized at the domain wall. Here, the global chiral symmetry is an inversion-like symmetry anticommuting with the finite Hamiltonian of a long enough subchain containing the domain wall. According to the explicit form of Γ, it exchanges the wavefunction amplitudes of two sites which are at an equal distance from the domain-wall center, accompanied by the appropriate sign change (see more details in Supplementary Note 1.5). Note that this global chiral symmetry is not a necessary but a sufficient condition for the existence of the zero-energy state. Therefore, an in-depth analysis, such as the robustness against a random disorder which breaks both chiral and global chiral symmetries, is required to claim that the numerically obtained zero-energy state is topological.

To see the robustness of the zero-energy domain-wall states under perturbations, we investigate the energy spectra in the presence of the onsite staggered quasi-periodic disorders for the three chains (Fig. 4a–c). The additional onsite potential at the ith site is given by $(-1)^i \lambda \cos(2\pi\beta i)$ with disorder strength λ and the inverse golden ratio β. The system size is chosen such that the onsite potential is nearly zero at the domain wall center, maintaining the topological phase transition for the SSH chain or a gapless phase transition condition for the AI chain, which will be elaborated on later. Such disorders are introduced as they are powerful enough to give random perturbations to the system[33,34]. Figure 4a–c shows the robustness of the zero-energy state of the AI chain to disorder, similar to that of the SSH chain, even in the absence of any global chiral symmetry that protects the zero-energy state, implying their topological nature. On the other hand, the RM domain-wall state fluctuates easily under the same disorder because it is not topologically protected.

To analytically confirm the origin and topological stability of the zero-energy domain-wall state, we adopt the Jackiw–Rebbi method introduced for explicitly analyzing the topological zero modes in the SSH model[26,27]. Following the method, we examine the low-energy effective continuum Hamiltonian for the generalized SSH model. We take the Dirac approximation at $k = -\frac{\pi}{2} + k'$, expand for a small k' regarding the Hamiltonian in Eq. (2), and upgrade the Δ and m_z as local functions considering the domain-wall configuration. Then, the effective continuum Hamiltonian is given as

$$H_{\mathrm{eff}} = 2t_0 k' \sigma_x + \Delta(x)\sigma_y + m_z(x)\sigma_z, \tag{3}$$

where $k' = -i\partial_x$ acts as the momentum operator in real space. Due to the last term, $m_z(x)\sigma_z$, which is a function of x and anti-commutes with the other terms, it is difficult to find a general Jackiw–Rebbi solution. Thus, we first consider a simpler case where $\xi_1 = \xi_2 = \xi$ and therefore $\Delta(x) = \Delta_0 \tanh(x/\xi)$, $m_z(x) = m_0 \tanh(x/\xi)$, with $\Delta_0 < 0$ and $m_0 < 0$. Then, the zero-energy solution localized at the domain wall center ($x = 0$) is given by

$$\psi(x) = \mathcal{N} e^{\mp \frac{1}{2t_0} \int_0^x dx' \sqrt{\Delta^2 + m_z^2}} \left(-\Delta_0 + \sqrt{\Delta_0^2 + m_0^2}, im_0 \right)^T,$$

where $\mathcal{N}$ is the normalization factor, the upper and lower signs indicate $x > 0$ and $x < 0$ regions, respectively, and $\Delta(x)$ and $m_z(x)$ are denoted as Δ and m_z for simplicity. We take a semi-infinite boundary condition for $x > 0$ and $x < 0$, with $\psi(x = \pm\infty) = 0$ and match the wavefunction at $x = 0$. This

zero-mode solution is identical to that of the SSH model when $m_z(x) = 0$[26,27]; $\psi(x) \propto e^{\frac{1}{2t_0}\int_0^x dx'\Delta(x')}(1,0)^T$. The analytical solution for the RM model is given by the same wavefuction[32]. These analytical solutions for the SSH, RM, and AI chains are also consistent with the numerically calculated wavefunction distributions, given in Fig. 2.

When solving Eq. (3), it should be noted that both $\Delta(x)$ and $m_z(x)$ must change their signs across the domain-wall center for the emergence of zero-energy Jackiw–Rebbi solutions. If we choose $m_z(x) = m_0|\tanh(x/\xi)|$ leaving the others same, the resulting zero-energy solution for each region is given as

$$\psi(x) = \mathcal{N} e^{\mp\frac{1}{2t_0}\int_0^x dx'\sqrt{\Delta^2+m_z^2}}\left(-\Delta_0 + \sqrt{\Delta_0^2+m_0^2}, \pm i m_0\right)^T,$$

where $\mathcal{N}$ is the normalization constant, the double signs are in order, and the upper signs indicate $x > 0$ while the lower signs indicate $x < 0$, respectively, and $\Delta(x)$ and $m_z(x)$ are denoted as Δ and m_z for simplicity. Such a zero-energy solution is not continuous at $x = 0$ and, therefore, is impossible. Topologically, this condition that both $\Delta(x)$ and $m_z(x)$ must change their signs across the domain wall is consistent with the quantization of the Berry phase difference of two interpolating domains, which will be discussed later.

To find a general solution to the zero-energy domain-wall states, we show that the low-energy effective Hamiltonian of Eq. (3) is equivalently transformed into that of the SSH model through an SU(2) unitary transformation. Using an unitary operator $U = \exp\left[-\frac{i}{2}\tan^{-1}\left(\frac{m_z(x)}{\Delta(x)}\right)\sigma_x\right]$, the continuum Hamiltonian in Eq. (3) is transformed into

$$H'_{\text{eff}} = (2t_0 k' + F)\sigma_x + \text{sgn}(\Delta)\sqrt{\Delta^2+m_z^2}\sigma_y, \tag{4}$$

where $k' = -i\partial_x$ is the momentum operator while $\Delta(x)$ and $m_z(x)$ are denoted as Δ and m_z for simplicity. $F(x) = -\partial_x t_0 \tan^{-1}\left(\frac{m_z(x)}{\Delta(x)}\right)$ rapidly converges to zero as $|x| \to \infty$ and is written as F for simplicity. This F term acts as a small oscillatory correction term, as shown in the zero-energy solution below. Hence, the F term does not change the topological nature of the zero-energy solution. Without loss of generality, we select $\Delta(-\infty) > 0$, $\Delta(+\infty) < 0$, $m_z(-\infty) > 0$, and $m_z(+\infty) < 0$. Then, the zero-energy solution $\psi'(x)$ is given by

$$\begin{aligned}\psi'(x) &= \mathcal{N}' e^{-\frac{1}{2t_0}\int_{x_c}^x dx'\left[iF(x') \pm \sqrt{\Delta(x')^2+m_z(x')^2}\right]}(1,0)^T, \\ &= \mathcal{N}' e^{\mp\frac{1}{2t_0}\int_{x_c}^x dx'\left[\sqrt{\Delta(x')^2+m_z(x')^2}\right] + \frac{i}{2}\tan^{-1}\left[\frac{m_z(x)}{\Delta(x)}\right]}(1,0)^T,\end{aligned}$$

where $\mathcal{N}'$ is the normalization factor, and the upper and lower signs indicate the $x > x_c$ and $x < x_c$ regions, respectively. Here, x_c is the domain-wall center where the sign of $\Delta(x)$ changes. The second term in Eq. (4) plays the role of $\Delta(x)$ of the SSH case[26,27]. Importantly, the transformed Hamiltonian in Eq. (4) has a generic chiral symmetry, $\{H'_{\text{eff}}, \sigma_z\} = 0$. Therefore, within the low-energy effective theory, the generalized SSH model is equivalent to the SSH model and protects zero-energy topological modes through the generic chiral symmetry.

Such Jackiw–Rebbi analysis also highlights the relation between the emergence of the zero-energy domain-wall state and the gap-closing phase transition point. In the SSH model, $\Delta(x)$ should experience the sign change within the domain wall for the convergence of the zero-energy solution mathematically, which implies the existence of a gap-closing phase transition point x_0 satisfying $\Delta(x_0) = 0$, where a zero-energy state is localized. Similarly, in the generalized SSH model, $\sqrt{\Delta(x)^2 + m_z(x)^2}$ should be zero within the domain wall due to the mathematical convergence of the zero-energy solution and boundary condition of wavefunctions, which implies that a topological state is localized at the gap-closing point where a phase transition occurs. If $\Delta(x)$ and $m_z(x)$ become zero at different positions along the chain, then there will be no zero-energy domain-wall states (Fig. 3).

Note that the existence of the gap-closing point along the chain is a necessary condition for the existence of zero-energy domain-wall states. If one adds a large on-site potential at the center of the domain wall, the energy of the domain-wall state will be shifted from zero. However, such a large on-site potential will result in the absence of a gap-closing point, which violates the necessary condition and hence is not allowed in this work.

Moreover, due to the topological stability of our domain-wall states, the details are also unimportant in the lattice system. We show that the zero-energy state is robust regardless of whether or not the gap-closing position x_c, which satisfies $\sqrt{\Delta(x_c)^2 + m_z(x_c)^2} = 0$, is at the center of an atom (see Fig. S4 for more details). Also, the zero-energy domain-wall state is stable even when two characteristic lengths are different (Fig. S2).

To further understand the topological nature of the zero-energy domain-wall state, we elaborate on the Berry phase difference between two corresponding domains and apply the bulk-boundary principle. The Berry phase difference is calculated from the Berry curvature by applying Stoke's theorem. Here, the Berry curvature is defined in 2D space-time, with the additional auxiliary time axis, i.e., the system is adiabatically transformed from one to another groundstate along the dotted lines seen in Fig. 2a as time passes (see more details in Supplementary Note 3). Figure 4d–f shows the calculated Berry curvature distributions for the three types of adiabatic evolution that correspond to the domain-wall configurations in Fig. 2a. The resulting Berry phase difference between the phases is quantized to π (arbitrary) for both the SSH and AI (RM) domain walls, which can be seen in Table 1. In the scope of the modern theory of polarization[28], the SSH and AI domain walls have quantized electric polarizations. Moreover, we can see the topological nature of the domain-wall states more clearly in the Berry curvature distributions in Fig. 4d–f; in the AI cases, the singular points in the Berry curvature indicate gap closing and mimics topological phase transition, similar to the SSH case. On the other hand, there is no such topological phase transition point in the RM case.

We suggest a guiding principle that extends the conventional bulk-boundary correspondence regarding topological domain-wall states. The essential quantity is not the Berry phase of each domain itself but the Berry

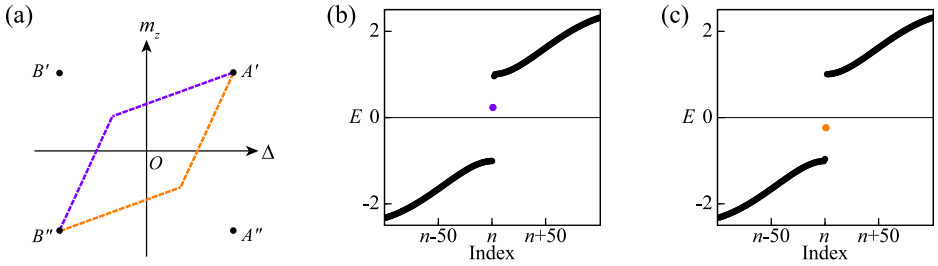

Fig. 3 | Two types of chains without crossing the gap closing point. a Schematics of two types of configurations connecting A' and B'' phases without crossing the gap closing point. The purple and orange lines indicate configurations with $x_1 < x_2$ and $x_1 > x_2$, respectively, where x_1 and x_2 are defined as the order-parameter-vanishing points satisfying $\Delta(x_1) = 0$ and $m_z(x_2) = 0$ for the energy-valued dimerization Δ and onsite energy m_z. Energy eigenvalues for the chain configurations along the **b** purple ($x_1 = 123, x_2 = 127$), and **c** orange ($x_1 = 127$, $x_2 = 123$) lines. The parameters are the same as the AI domain-wall configuration of Fig. 2.

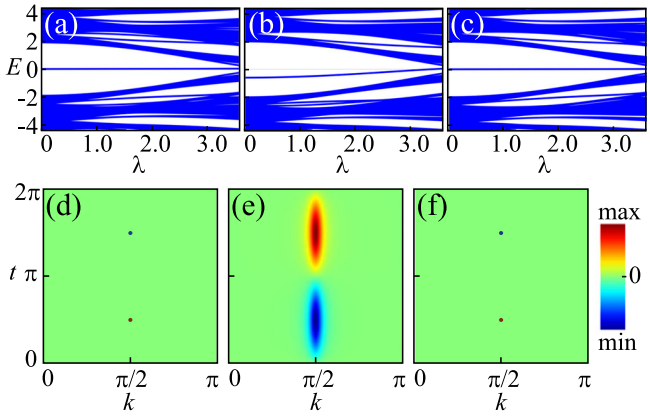

Fig. 4 | Response to disorder and the Berry curvature for the generalized Su–Schrieffer–Heeger (SSH) models. The energy eigenvalues with respect to the quasi-periodic disorder strength λ for the **a** SSH, **b** Rice–Mele (RM), and **c** AI domain-wall configurations. Normalized Berry curvature distributions for the **d** SSH, **e** RM, and **f** AI systems under the adiabatic evolution time parameter (t). The parameters are the same as in Fig. 2.

Table 1 | Quantized Berry phase differences between two groundstates in generalized Su–Schrieffer–Heeger (SSH) models

	Berry phase difference
SSH	π
RM	0.61π
A	π
AI	π
AII	(π, π)

All cases, except for the Rice-Mele (RM) domain wall, exhibit quantized values of π and manifest zero-energy domain-wall states, consistent with the principles of the extended bulk-boundary correspondence. The corresponding distributions of Berry curvature can be found in Figs. 2d–f and S1c, f for SSH, RM, AI, A, and AII domain walls, respectively. For the spinful AII class, two values enclosed in parentheses represent results for individual up and down spins.

phase difference between two domains that create the domain wall, as shown in Fig. 1b, c. Such a principle can be easily applied to the SSH domain-wall configurations and the corresponding topological domain wall state. As shown in Fig. 2a, the Berry phase of the topologically trivial A groundstate is zero while that of the non-trivial B groundstate is π, which endows the zero-energy domain-wall state in the SSH model due to the bulk-boundary principle. On the other hand, for the AI systems, the four groundstates (A', A'', B', B'') have Berry phases which are non-zero but also not π. Therefore, to have a topological domain wall, two groundstates with $\Delta\phi = \pi$ need to form a domain wall. For the blue and green lines of Fig. 2a, it can be seen that the value of $\Delta\phi$ will be $\pi - 2\delta$ and π, respectively, and therefore only the domain-wall configuration of the green line will have topological domain-wall states, which is consistent with the results that we have given. Therefore, the quantized Berry phase difference and the gap-closing phase transition guarantee the topological zero-energy domain-wall state. This indicates that even for seemingly trivial classes, zero-energy domain-wall states can emerge, which extends the conventional bulk-boundary correspondence.

Generalization to superconducting systems

We extend our concept and method from electronic to superconducting systems. Like the SSH chain, the Kitaev chain[35] is one prototypical system that hosts topological zero-energy boundary states (i.e., Majorana fermions) (Fig. 5a). It is a spinless single-orbital fermionic lattice tight-binding model with the nearest-neighbor hopping t, and p-wave superconducting pairing potential Δ_p. The Bloch Bogliubov-de-Gennes (BdG) Hamiltonian is given as

$$H_{\mathrm{BDI}}(k) = -\left(2t\cos k + \mu\right)\tau_z + 2\Delta_p \sin k\tau_y, \tag{5}$$

where the Pauli matrices τ_i indicates the Nambu space and μ is the onsite chemical potential. The Hamiltonian H_{BDI} has time-reversal ($T = K$), particle–hole ($C = \tau_x K$), and chiral ($\Gamma = \tau_x$), implying the topological BDI class in the tenfold classification table (Fig. 1(a)) because $T^2 = C^2 = 1$. The system is topological when $|\mu|<|2t|$, and trivial otherwise. Therefore, two groundstates are topologically distinguishable, and a domain-wall configuration connecting them generates a topological zero-energy Majorana fermion (Fig. 5a).

On the contrary, we now introduce the minimal spinless model belonging to the topologically trivial CI class as a representative model among the superconducting classes in Fig. 1a. This model will be denoted as the generalized Kitaev model. Unlike the conventional Kitaev chain utilizing p-wave pairing potential only, we consider both s- and p-wave pairing potentials to examine the existence of the Majorana zero modes. The model is essentially a two-orbital model, which will be discussed later. Thus, the model Hamiltonian H_{CI} is comprised of three parts H_n, H_s, and H_p which are normal state, s- and p-wave pairing Hamiltonians (Fig. 5b):

$$\begin{aligned}
H_{\mathrm{CI}} &= H_n + H_s + H_p,\\
H_n &= \sum_{\gamma,j} -t\left(c^\dagger_{\gamma,j}c_{\gamma,j+1} + c^\dagger_{\gamma,j+1}c_{\gamma,j}\right) - \mu c^\dagger_{\gamma,j}c_{\gamma,j},\\
H_s &= \sum_{j} \Delta_s\left(-c_{1,j}c_{2,j} + c_{2,j}c_{1,j}\right) + h.c.,\\
H_p &= \sum_{\gamma,j} \Delta_p\left(c_{\gamma,j+1}c_{\gamma+1,j} - c_{\gamma,j}c_{\gamma+1,j+1}\right) + h.c.,
\end{aligned}$$

where $c^\dagger_{\gamma,j}/c_{\gamma,j}$ indicates the creation/annihilation operator for orbital $\gamma = 1, 2$ at site j. Here, μ, t, Δ_s, and Δ_p are the chemical potential, nearest-neighbor hopping parameter, and s- and p-wave pairing gaps, respectively. Thus, the Bloch BdG Hamiltonian in the basis of $(c^\dagger_1, c^\dagger_2, c_1, c_2)$ is given by

$$H_{\mathrm{CI}}(k) = -\left(2t\cos k + \mu\right)\tau_z + \Delta_s\tau_y\sigma_y + 2\Delta_p \sin k\tau_y\sigma_x, \tag{6}$$

where the Pauli matrices τ_i and σ_j indicate the Nambu space and orbital degrees of freedom. Generally, when $\Delta_s \neq 0$, the Hamiltonian $H_{\mathrm{CI}}(k)$ has time-reversal ($T = K$), particle–hole ($C = \tau_y\sigma_z K$), and chiral ($\Gamma = \tau_y\sigma_z$) symmetries, implying the CI class; $T^2 = 1$ and $C^2 = -1$. On the other hand, when $\Delta_s = 0$, the Hamiltonian $H_{\mathrm{CI}}(k)$ is equivalent to two independent Kitaev Hamiltonians $H_{\mathrm{BDI}}(k)$ in Eq. (5) because $H_{\mathrm{CI}}(k)$ can be block-diagonalized according to the eigenvalues of σ_x in the last term of $H_{\mathrm{CI}}(k)$ and each subblock Hamiltonian is of the form of the Kitaev model. Moreover, in each Kitaev Hamiltonian, $C' = \tau_x K$ with $C'^2 = 1$ plays the role of the particle–hole symmetry operator, implying the topological BDI class. For this reason, when $\Delta_s = 0$, we denote the generalized Kitaev model as a double Kitaev (DK) model. For convenience, when $\Delta_s = \mathrm{const.}$, we denote the generalized Kitaev model as a constant s-wave (CSW) model. In this case, the constant Δ_s term anticommutes with the other terms of the Hamiltonian, therefore acting as a Dirac mass term.

Unlike the Kitaev model described by the 2×2 BdG Hamiltonian, the simplest representation of the CI class is a 4×4 matrix BdG Hamiltonian (i.e., two-orbital model) due to the Fermi statistics, $\Delta(k)^T = -\Delta(-k)$, and symmetry constraints of the particle–hole symmetry, $CH(k)C^{-1} = -H(-k)$, which forbids the presence of s- and p-wave pairings for a 1D chain within a 2×2 BdG Hamiltonian (see details in Supplementary Note 2.1). Note that the Hamiltonian in Eq. (6) is generic because symmetry analysis forbids pairing terms that are proportional to neither $\tau_y\sigma_y$ nor $\tau_y\sigma_x$.

We now discuss the degenerate groundstates and the domain-wall state connecting them. For simplicity, we focus on the physics near the Fermi level (that is, near $k = 0$), where the superconducting gap opens. Moreover,

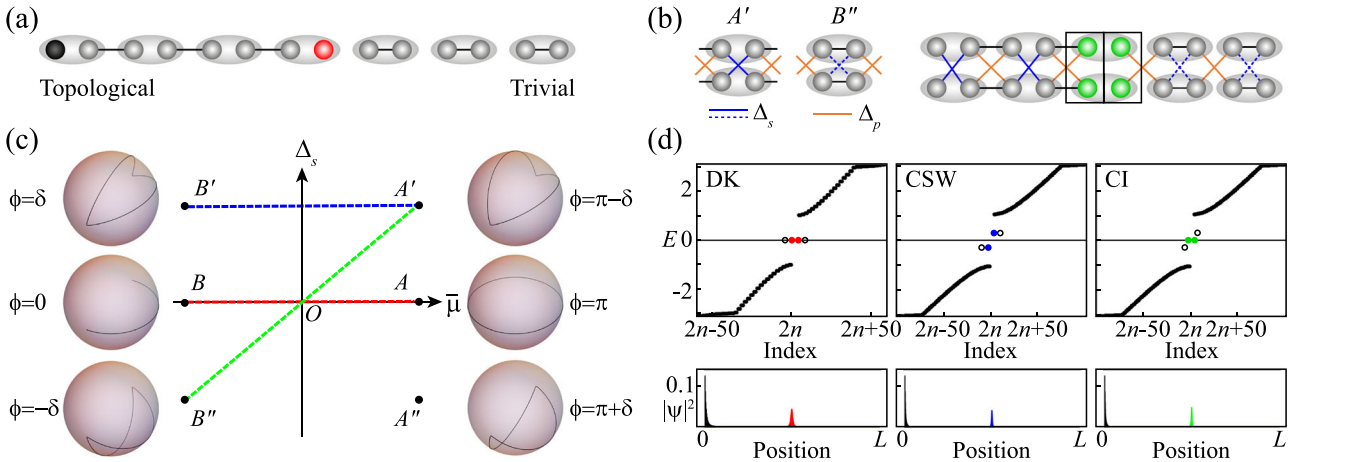

Fig. 5 | Generalized Kitaev chains. a Schematics for a domain-wall configuration for the Kitaev chain in the Majorana fermion representation, where the gray oval indicates a fermion in the physical lattice, and the spheres inside indicate Majorana fermions. The domain-wall configuration connects from topological to trivial groundstates, where the black (red) sphere indicates a zero-energy Majorana fermion localized on the left edge (at the center) of each chain. **b** Schematics for two groundstates and a domain-wall configuration for the CI chain in the Majorana fermion representation. The blue and orange lines indicate *s*- and *p*-wave pairings, respectively; solid (dotted) lines indicate a positive (negative) expectation value. For simplicity, the black lines represent the effects of the chemical potential and hopping. The squares with two green circles each indicate Majorana states localized at the center of the chain. **c** Order-parameter space composed of the redefined chemical potential ($\bar{\mu} = \mu + 2t$) and *s*-wave pairing function (Δ_s). The black line in each Bloch sphere indicates the trajectory of the *d* vector for each groundstate. ϕ indicates the value of the Berry phase of each groundstate, where δ is a positive number. The red, blue, and green dotted lines indicate the double Kitaev (DK), constant *s*-wave (CSW), and CI chains. **d** Energy eigenvalues and the wavefunctions of the corresponding ingap states for DK, CSW, and CI chains. The ingap states are distinguished by the colors and magnified by two for clarity. The DK and CI chains show topological zero-energy domain-wall states indicated by red and green. On the other hand, the CSW chain shows non-zero-energy domain-wall states with $E = \pm\Delta_s$ indicated by blue. For the edge states indicated by black open circles, the CSW and CI chains exhibit non-zero-energy edge states with $E = \pm\Delta_s$, while only the DK chain shows topological zero-energy edge states. For all three cases, the hopping parameter and *p*-wave pairings are fixed at $t = 1$, $\Delta_p = 10$, respectively, and the chemical potential μ is interpolated from 1 to −5. The characteristic length is $\xi = 5$, and the number of sites is $L = 4n = 1600$. The *s*-wave pairing term is fixed at 0, 0.3, or interpolated from 0.3 to −0.3 for the DK, CSW, and CI chains, respectively.

we take a limit of large Δ_p where the *p*-wave dispersion is more dominant than the electronic dispersion $2t\cos k$, i.e., a degenerate limit. Then, the energy eigenvalue of Eq. (6) is given by $E = \pm\sqrt{\bar{\mu}^2 + \Delta_s^2 + 4\Delta_p^2\sin^2 k}$, where $\bar{\mu} = \mu + 2t$ is an redefined chemical potential. Depending on $\bar{\mu}$ and Δ_s, there exist various groundstates, which indicates that $\bar{\mu}$ and Δ_s act as our order parameters of the system with a fixed Δ_p (Fig. 5c). For $\Delta_s = 0$, there exist two degenerate groundstates A and B, which are of the BDI class as discussed before. On the other hand, when $\Delta_s \neq 0$, the combination of Δ_s and $\bar{\mu}$ make up four energetically degenerate groudstates (A', B', A'', B'') depending on the signs of $\bar{\mu}$ and Δ_s, as shown in Fig. 5c.

We now consider three types of domain-wall configurations connecting groundstates; $A \to B$, $A' \to B'$, and $A' \to B''$, given by the red, blue, and green dotted lines in Fig. 5c, respectively. We denote these three domain-wall configurations as the double Kitaev (DK), constant *s*-wave (CSW), and CI chains, respectively. If $\Delta_s(x) = 0$ throughout the chain and the redefined chemical potential varies as $\bar{\mu}(x) = \mu_0\tanh(x/\xi)$ connecting the A and B groundstates, the domain-wall configuration becomes the DK chain. Here, ξ is the characteristic length of the domain wall. The DK chain is equivalent to two independent Kitaev chains because the DK chain Hamiltonian can also be block-diagonalized, as discussed before. Moreover, when $\Delta_s(x)$ is additionally interpolated, such as $\Delta_s(x) = \Delta_{s,0}\tanh(x/\xi)$, the CI domain-wall configuration connecting A' and B'' groundstates emerges, which can be seen in Fig. 5b. Without loss of generality, we take the characteristic lengths of the order parameters of $\bar{\mu}(x)$ and $\Delta_s(x)$ to be equal. Note that even if the characteristic lengths are different, there would be no significant difference regarding the topological zero-energy domain-wall states for the CI chain, as discussed in the case of the generalized SSH chain; solving the effective Hamiltonian in Eq. (8) allows the general solution independent of the details to be obtained, which is discussed later. For comparison, the CSW domain-wall configuration connecting A' and B' groundstates (Fig. S5(b)) is also considered where $\Delta_s(x) = \Delta_{s,0} = \text{const.}$, which prohibits a zero-energy state. That is, due to Δ_s behaving as a Dirac mass term, the energy eigenvalues of the ingap states are given as $E = \pm\Delta_{s,0}$, similar to the RM chain (see more details in Supplementary Note 2.2). Therefore, the DK, CSW, and CI chains are comparable to the SSH, RM, and AI chains in the electronic systems, respectively.

The energy spectra for the three domain-wall configurations are shown in Fig. 5d; the DK and CSW domain-wall states are located at zero and non-zero, respectively, as expected. On the other hand, unexpected Majorana zero-energy modes emerge in the CI domain-wall states. To compare the domain-wall states with the usual edge states, we also investigate the ingap states localized at the left edge for the three cases (Fig. 5d). For the DK case, the left edge states are zero-energy ingap states. On the other hand, for the CSW and CI cases, the left edge states are non-zero in-gap states located at $E = \pm\Delta_s$, which can be seen as in-gap states split by the Dirac mass term Δ_s. Note that, for the conventional Kitaev chain case, there are two zero-energy ingap states, which are each localized at the domain wall and the left edge, as can be seen in Fig. S7a.

The stability of the zero-energy Majorana domain-wall states is examined using a similar onsite quasi-periodic disorder used for the generalized SSH cases[33,34]. The additional onsite potential at orbital $\gamma = 1, 2$ at site i is given by $\pm(-1)^{\gamma}\lambda\cos(2\pi\beta i)$ with disorder strength λ and the inverse golden ratio β, where the positive and negative overall signs indicate the disorders in the electron and hole parts of the BdG Hamiltonian, respectively. As shown in Fig. 6a–c, the domain-wall states for the DK and CI chains show robustness against random disorder, similar to the conventional Kitaev model of Fig. S7b, while that of CSW does not.

Using a corresponding low-energy effective Hamiltonian to the generalized Kitaev Hamiltonian in Eq. (6) and the Jackiw–Rebbi method, we analyze the origin and topological stability of the Majorana zero-energy domain-wall state. Taking the Dirac approximation at $k = 0$, the effective Hamiltonian is obtained as

$$H_{\text{eff}}^{\text{CI}} = -\bar{\mu}(x)\tau_z + \Delta_s(x)\tau_y\sigma_y + 2\Delta_p k\tau_y\sigma_x, \tag{7}$$

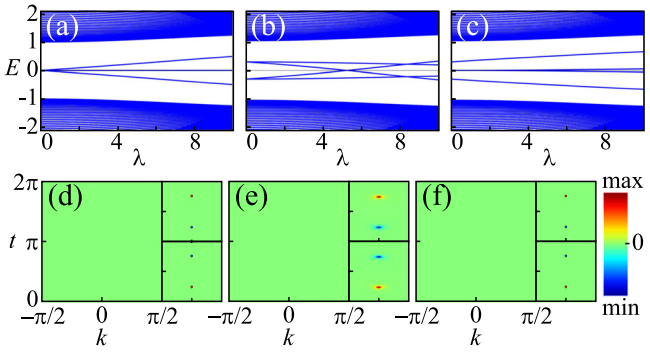

Fig. 6 | Response to disorder and the Berry curvature for the generalized Kitaev models. Energy eigenvalues for the **a** double Kitaev (DK), **b** constant *s*-wave (CSW), and **c** CI domain-wall configurations with respect to the disorder strength λ. The energy eigenvalues for $\lambda = 0$ are equal to the energy eigenvalues given in Fig. 5d. In **a**, **c**, the topological zero-energy domain-wall states are stable for reasonable strength of disorders, while the two edge states spread out as λ increases because the disorder hybridizes two edge states. In **b**, all ingap states are not robust out as λ increases because they are non-topological. Normalized Berry curvature distributions for the **d** DK, **e** CSW, and **f** CI systems under the adiabatic evolution time parameter (t). Berry curvature distributions for the subblocks are given on the right. In **d**, **f**, the sharp points indicate the singular point where the gap is closed and a topological phase transition occurs. The Berry curvature is blurred in (**e**), implying no topological phase transition and non-quantization of the Berry phase difference. The parameters and the domain-wall configurations are the same as in Fig. 5.

where $k = -i\partial_x$ in the real space. For simplicity, the spatial functions, $\bar{\mu}(x)$ and $\Delta_s(x)$ are denoted as $\bar{\mu}$ and Δ_s. Due to $\bar{\mu}(x)$ and $\Delta_s(x)$ both being x-dependent, it is difficult to find a general Jackiw–Rebbi solution. Thus, we consider a simpler case where $\bar{\mu}(x) = \mu_0 \tanh(x/\xi)$ and $\Delta_s(x) = \Delta_0 \tanh(x/\xi)$ with $\mu_0 < 0$ and $\Delta_0 < 0$ without loss of generality. Note that the solution for the general $\bar{\mu}(x)$ and $\Delta_s(x)$ is given below. The two resulting zero-energy domain-wall solutions are

$$\psi_i(x) = \mathcal{N} \exp\left[\mp \frac{1}{2\Delta_p} \int_0^x dx' \sqrt{\Delta_s^2 + \bar{\mu}^2}\right] \phi_i,$$

where $\mathcal{N}$ is the normalization factor, $i = 1, 2$, and the upper and lower signs indicate $x > 0$ and $x < 0$ regions, respectively. The x-independent ϕ_i is given by

$$\phi_1 = \left(-\Delta_{s,0} + \sqrt{\Delta_{s,0}^2 + \mu_0^2}, 0, 0, \mu_0\right)^T,$$
$$\phi_2 = \left(0, \mu_0, -\Delta_{s,0} + \sqrt{\Delta_{s,0}^2 + \mu_0^2}, 0\right)^T.$$

The two wavefunctions at zero energy are degenerate and form Majorana pairs in the simplified forms

$$\Psi_\pm(x) = \psi_1(x) \pm \psi_2(x),$$

satisfying the Majorana condition of $\Psi_\pm^c = \Psi_\pm$. This analytically obtained wavefunction is consistent with the wavefunctions obtained numerically using the tight-binding method in Figs. 5d and S5d. It should be noted that similar to the Jackiw–Rebbi solution to Eq. (3), for ϕ_1 and ϕ_2 to be continuous, a sign change of $\bar{\mu}(x)$ and $\Delta_s(x)$ must occur at $x = 0$. This is also consistent with the guiding principle regarding the Berry phase of two interpolating states to be quantized.

Similar to the case of the generalized SSH model, to find a general solution to the zero-energy domain-wall states, Eq. (7) is equivalently transformed into that of the Kitaev model through an SU(4) transformation. Under a SU(4) unitary transformation via unitary operator $U = \exp\left[\frac{i}{2}\left(\frac{\pi}{2}\tau_0 + \tan^{-1}\left(\frac{\Delta_s(x)}{\bar{\mu}(x)}\right)\tau_x\right)\sigma_y\right]$, the effective Hamiltonian is transformed into

$$H_{\text{eff}}^{\text{CI}'} = -\,\text{sgn}\,(\bar{\mu})\sqrt{\bar{\mu}^2 + \Delta_s^2}\,\tau_z + \left(2\Delta_p k + F\right)\tau_y\sigma_z, \tag{8}$$

where $k = -i\partial_x$ is the momentum operator while $\bar{\mu}(x)$ and $\Delta_s(x)$ are denoted as $\bar{\mu}$ and Δ_s for simplicity. $F(x) = -\partial_x\Delta_p \tan^{-1}\left(\frac{\Delta_s(x)}{\bar{\mu}(x)}\right)$ rapidly converges to zero as $|x| \to \infty$ and is written as F for simplicity. This F term, as was the case of the SSH model, acts as an oscillation term and, therefore, does not affect the topological nature of the zero-energy solution. Note that the Hamiltonian in Eq. (8) is that of the two independent Kitaev models because this Hamiltonian can be block-diagonalized depending on the eigenvalue of σ_z and each subblock Hamiltonian is the effective Hamiltonian of the Kitaev chain.

Without loss of generality, we select $\bar{\mu}(+\infty)<0$, $\bar{\mu}(-\infty)>0$, $\Delta_s(+\infty) < 0$, and $\Delta_s(-\infty) > 0$. Then, the Jackiw–Rebbi zero-energy solution of this Hamiltonian is given by

$$\psi_1^{\text{eff}}(x) = \mathcal{N}' \exp\left[-\frac{\int^x dx' iF(x') \pm \sqrt{\Delta_s(x')^2 + \bar{\mu}(x')^2}}{2\Delta_p}\right](-1, 0, 1, 0)^T,$$
$$\psi_2^{\text{eff}}(x) = \mathcal{N}' \exp\left[-\frac{\int^x dx' iF(x') \pm \sqrt{\Delta_s(x')^2 + \bar{\mu}(x')^2}}{2\Delta_p}\right](0, 1, 0, 1)^T,$$

where $\mathcal{N}'$ is the normalization factor, and the upper and lower signs indicate the $x > 0$ and $x < 0$ regions, respectively. These wavefunctions are, as expected, indicates Majorana fermions. Our zero-energy solution is topological as it is independent of the precise form of $\bar{\mu}(x)$ and $\Delta_s(x)$. It only depends on the sign change of $\bar{\mu}(x)$ and $\Delta_s(x)$ across the domain wall, and the Hamiltonian of Eq. (8) is similar to that of the conventional Kitaev model. It can be seen that the first term of Eq. (8) plays the role of the chemical potential in the conventional Kitaev chain. Moreover, the Hamiltonian $H_{\text{eff}}^{\text{CI}'}$ has time-reversal ($T = K$), particle–hole ($C = \tau_x K$), and chiral ($\Gamma = \tau_x$) symmetries, implying the BDI class. As was the case for the generalized SSH model, $\sqrt{\bar{\mu}^2 + \Delta_s^2}$ should be zero within the domain wall for the emergence of the zero-energy Majorana domain-wall states due to the convergence and boundary conditions of the wavefunction of the domain-wall states. This is consistent with the gap-closing phase-transition condition.

Ascending from the low-energy limit and considering the full Hamiltonian, the Berry phase, and as a result, the extended bulk-boundary correspondence is used to explore the topological nature of the Majorana zero-energy domain-wall states further. Usually, a winding number describes the topological order of a superconducting system[1,2]. Equivalently, the Berry/Zak phase can be applied[24,25,36]. Similar to the generalized SSH model, the Berry curvature is defined in 2D space-time, and from the Berry curvature, the Berry phase difference between the two domains is obtained. Figure 6d–f shows the calculated Berry curvature for the three domain-wall configurations given in Fig. 5c. The Berry curvature for all three cases is zero, implying no change in the Berry phase. However, under a basis change of $(c_1^\dagger, c_2^\dagger, c_1, c_2) \to (c_1^\dagger, c_2, c_2^\dagger, c_1)$, $H_{\text{CI}}(k)$ can be block-diagonalized as

$$H'_{\text{CI}}(k) = -\left(2t\cos k + \mu\right)\sigma_z + \Delta_s\tau_z\sigma_x + 2\Delta_p \sin k\tau_z\sigma_y,$$

which is grouped into subblocks according to the τ_z eigenvalues. As seen from the electron–hole picture (Fig. S6a), such basis change is allowed due to the interacting configuration within the model. It is for this Hamiltonian $H'_{\text{CI}}(k)$, where the d vector for the groundstates shown in Fig. 5c is defined via $H'_{\text{CI}}(k) = \tau_z(d_x\sigma_x + d_y\sigma_y) + d_z\sigma_z$. The Berry phases of individual subblocks are now examined. The subblocks for the DK and CI domain-wall systems have a quantized Berry phase difference of π and gap closing in the degenerate limit, similar to the conventional Kitaev system as shown in Fig. S7c. Regarding the subblocks for the CSW domain-wall system, the

Table 2 | Quantized Berry phase differences for the generalized Kitaev models

	Total	Subblock 1	Subblock 2
Kitaev	π	NA	NA
DK	0	π	$-\pi$
CSW	0	0.94π	-0.94π
CI	0	π	$-\pi$
C	0	π	$-\pi$
$\widetilde{\mathrm{C}}$	0	π	$-\pi$

All cases, except for the Kitaev model, exhibit a total Berry phase difference of zero. On the other hand, with the exception of the constant *s*-wave (CSW) case, the quantization of Berry phases is observed within their respective subblock for double Kitaev (DK), CI, C, and $\widetilde{\mathrm{C}}$ cases. Consequently, these cases adhere to a extended bulk-boundary correspondence. Detailed Berry curvature distributions can be found in Figs. 5d–f, S6d, g, and S7c for DK, CSW, CI, C, $\widetilde{\mathrm{C}}$, and Kitaev systems, respectively.

Berry phase difference is not quantized, indicating that the topological zero-energy state is forbidden (Table 2). As was the case for the generalized SSH model, Majorana zero-energy domain-wall states can also emerge in seemingly trivial systems via our extended bulk-boundary correspondence.

Conclusion

So far, the discussion has focused on the generalized SSH and Kitaev models for the AI and CI classes. Regarding the other three classes (A, AII, C), the methodology and the results thereafter are similar to those of the AI (for A, AII) or CI (for C) classes, which can be seen in the Supplementary Notes 1 and 2, respectively. We, therefore, conclude that even systems classified as trivial can possess zero-energy topological domain-wall states. Physical realization of such systems inevitably results in quantized electric polarization for the generalized SSH model and Majorana zero modes for the generalized Kitaev models. Our results are for the simplest model possible, however, there is no loss of generality, and the extensions will be numerous. For instance, both spinless and spinful models for the A class are suggested in Supplementary Note 1, and two generalized Kitaev models are suggested for the C class in Supplementary Note 2.

The realization of the generalized SSH model is expected in various 1D electronic systems where the tuning of parameters and generating a domain wall is relatively easier, e.g., atomic nanowires[37,38], artificial electronic lattices[39,40], graphene nanoribbons[41,42], optical and plasmonic systems[9,10], etc. Application for the generalized Kitaev model is also expected in superconducting systems, e.g., proximity-effect-induced superconductors[43–47] and hybrid 1D superconductors[48–50]. As these domain-wall states are points, it could be possible to realize such domain-wall states in higher-order topological systems[51–55]. Besides closed systems, our idea can also be applied to non-hermitian and open systems[56–59]. Expanding on our findings and their realization could open new platforms in topological science, with potential applications in quantum computation and topological devices, including topological lasers[10,13,14].

Methods

The tight-binding method was used to calculate the numerical results of the domain-wall configurations for both electronic and superconducting systems. For analytical results, the Jackiw–Rebbi formalism is used. For Majorana fermion representation in Fig. 5, the relation for the ith Majorana fermion operator at the γ orbital of the jth site, $a_{i,\gamma,j}$, is given by

$$a_{1,\gamma,j}=\frac{1}{\sqrt{2}}\left(c_{\gamma,j}+c_{\gamma,j}^{\dagger}\right),\ a_{2,\gamma,j}=-\frac{i}{\sqrt{2}}\left(c_{\gamma,j}-c_{\gamma,j}^{\dagger}\right),$$

where $c_{\gamma,j}^{\dagger}$ and $c_{\gamma,j}$ indicate the creation and annihilation operators for the electron at the γ orbital of the jth site.

The Berry curvature of the generalized SSH and Kitaev models are calculated using a cyclic adiabatic time evolution of a 1D Hamiltonian $H(k,\tau)$ with a time τ. This 1D lattice system is expanded into a 2D lattice system by considering the time τ as an extra dimension. This allows the derivation of a Berry curvature along k and τ, leading to the Berry phase of the domain-wall configurations given in Tables 1 and 2. Further details can be found in Supplementary Note 3.

Data availability

The data used in this paper are available from M.J.P. or S.C. on reasonable request.

Received: 8 February 2024; Accepted: 5 July 2024;
Published online: 17 July 2024

References

1. Schnyder, A. P., Ryu, S., Furusaki, A. & Ludwig, A. W. Classification of topological insulators and superconductors in three spatial dimensions. *Phys. Rev. B* **78**, 195125 (2008).
2. Chiu, C.-K., Teo, J. C., Schnyder, A. P. & Ryu, S. Classification of topological quantum matter with symmetries. *Rev. Mod. Phys.* **88**, 035005 (2016).
3. Qi, X.-L. & Zhang, S.-C. Topological insulators and superconductors. *Rev. Mod. Phys.* **83**, 1057 (2011).
4. Hasan, M. Z. & Kane, C. L. Colloquium: topological insulators. *Rev. Mod. Phys.* **82**, 3045 (2010).
5. He, Q. L., Hughes, T. L., Armitage, N. P., Tokura, Y. & Wang, K. L. Topological spintronics and magnetoelectronics. *Nat. Mater.* **21**, 15–23 (2022).
6. Tokura, Y., Yasuda, K. & Tsukazaki, A. Magnetic topological insulators. *Nat. Rev. Phys.* **1**, 126–143 (2019).
7. Atala, M. et al. Direct measurement of the Zak phase in topological Bloch bands. *Nat. Phys.* **9**, 795–800 (2013).
8. Cooper, N., Dalibard, J. & Spielman, I. Topological bands for ultracold atoms. *Rev. Mod. Phys.* **91**, 015005 (2019).
9. Meier, E. J., An, F. A. & Gadway, B. Observation of the topological soliton state in the Su–Schrieffer–Heeger model. *Nat. Commun.* **7**, 13986 (2016).
10. Ozawa, T. et al. Topological photonics. *Rev. Mod. Phys.* **91**, 015006 (2019).
11. Zhou, X.-F. et al. Dynamically manipulating topological physics and edge modes in a single degenerate optical cavity. *Phys. Rev. Lett.* **118**, 083603 (2017).
12. Zeng, L.-S., Shen, Y.-X., Peng, Y.-G., Zhao, D.-G. & Zhu, X.-F. Selective topological pumping for robust, efficient, and asymmetric sound energy transfer in a dynamically coupled cavity chain. *Phys. Rev. Appl.* **15**, 064018 (2021).
13. Nayak, C., Simon, S. H., Stern, A., Freedman, M. & Das Sarma, S. Non-Abelian anyons and topological quantum computation. *Rev. Mod. Phys.* **80**, 1083–1159 (2008).
14. Stern, A. & Lindner, N. H. Topological quantum computation-from basic concepts to first experiments. *Science* **339**, 1179–1184 (2013).
15. Shiozaki, K. & Sato, M. Topology of crystalline insulators and superconductors. *Phys. Rev. B* **90**, 165114 (2014).
16. Cornfeld, E. & Chapman, A. Classification of crystalline topological insulators and superconductors with point group symmetries. *Phys. Rev. B* **99**, 075105 (2019).
17. Khalaf, E., Po, H. C., Vishwanath, A. & Watanabe, H. Symmetry indicators and anomalous surface states of topological crystalline insulators. *Phys. Rev. X* **8**, 031070 (2018).
18. Yang, B.-J. & Nagaosa, N. Classification of stable three-dimensional Dirac semimetals with nontrivial topology. *Nat. Commun.* **5**, 4898 (2014).
19. Armitage, N., Mele, E. & Vishwanath, A. Weyl and Dirac semimetals in three-dimensional solids. *Rev. Mod. Phys.* **90**, 015001 (2018).
20. Wang, Z. et al. Sub-symmetry-protected topological states. *Nat. Phys.* **19**, 992–998 (2023).
21. Guo, C. et al. Quasi-symmetry-protected topology in a semi-metal. *Nat. Phys.* **18**, 813–818 (2022).

22. Haldane, F. Berry curvature on the fermi surface: anomalous hall effect as a topological fermi-liquid property. *Phys. Rev. Lett.* **93**, 206602 (2004).
23. Teo, J. C. Y. & Kane, C. L. Topological defects and gapless modes in insulators and superconductors. *Phys. Rev. B* **82**, 115120 (2010).
24. Berry, M. V. Quantal phase factors accompanying adiabatic changes. *Proc. R. Soc. Lond. A Math. Phys. Sci.* **392**, 45–57 (1984).
25. Zak, J. Berry's phase for energy bands in solids. *Phys. Rev. Lett.* **62**, 2747–2750 (1989).
26. Jackiw, R. & Rebbi, C. Solitons with fermion number 1/2. *Phys. Rev. D.* **13**, 3398–3409 (1976).
27. Jackiw, R. & Schrieffer, J. R. Solitons with fermion number $\frac{1}{2}$ in condensed matter and relativistic field theories. *Nucl. Phys. B* **190**, 253–265 (1981).
28. Resta, R. Modern theory of polarization in ferroelectrics. *Ferroelectrics* **151**, 49–58 (1994).
29. Qi, X.-L., Hughes, T. L. & Zhang, S.-C. Topological field theory of time-reversal invariant insulators. *Phys. Rev. B* **78**, 195424 (2008).
30. Han, S.-H., Jeong, S.-G., Kim, S.-W., Kim, T.-H. & Cheon, S. Topological features of ground states and topological solitons in generalized Su-Schrieffer-Heeger models using generalized time-reversal, particle-hole, and chiral symmetries. *Phys. Rev. B* **102**, 235411 (2020).
31. Su, W. P., Schrieffer, J. R. & Heeger, A. J. Solitons in polyacetylene. *Phys. Rev. Lett.* **42**, 1698–1701 (1979).
32. Rice, M. J. & Mele, E. J. Elementary excitations of a linearly conjugated diatomic polymer. *Phys. Rev. Lett.* **49**, 1455–1459 (1982).
33. Roy, S., Mishra, T., Tanatar, B. & Basu, S. Reentrant localization transition in a quasiperiodic chain. *Phys. Rev. Lett.* **126**, 106803 (2021).
34. Roy, S., Nabi, S. N. & Basu, S. Critical and topological phases of dimerized kitaev chain in presence of quasiperiodic potential. *Phys. Rev. B* **107**, 014202 (2023).
35. Kitaev, A. Y. Unpaired Majorana fermions in quantum wires. *Physica* **44**, 131 (2001).
36. Viyuela, O., Vodola, D., Pupillo, G. & Martin-Delgado, M. A. Topological massive Dirac edge modes and long-range superconducting Hamiltonians. *Phys. Rev. B* **94**, 125121 (2016).
37. Cheon, S., Kim, T.-H., Lee, S.-H. & Yeom, H. W. Chiral solitons in a coupled double Peierls chain. *Science* **350**, 182–185 (2015).
38. Kim, T.-H., Cheon, S. & Yeom, H. W. Switching chiral solitons for algebraic operation of topological quaternary digits. *Nat. Phys.* **13**, 444–447 (2017).
39. Drost, R., Ojanen, T., Harju, A. & Liljeroth, P. Topological states in engineered atomic lattices. *Nat. Phys.* **13**, 668–671 (2017).
40. Huda, M. N., Kezilebieke, S., Ojanen, T., Drost, R. & Liljeroth, P. Tuneable topological domain wall states in engineered atomic chains. *Npj Quantum Mater.* **5**, 17 (2020).
41. Li, J. et al. Topological phase transition in chiral graphene nanoribbons: from edge bands to end states. *Nat. Commun.* **12**, 5538 (2021).
42. Gröning, O. et al. Engineering of robust topological quantum phases in graphene nanoribbons. *Nature* **560**, 209–213 (2018).
43. Fu, L. & Kane, C. L. Superconducting proximity effect and Majorana fermions at the surface of a topological insulator. *Phys. Rev. Lett.* **100**, 096407 (2008).
44. Nakosai, S., Tanaka, Y. & Nagaosa, N. Two-dimensional p-wave superconducting states with magnetic moments on a conventional s-wave superconductor. *Phys. Rev. B* **88**, 180503 (2013).
45. Stanescu, T. D., Sau, J. D., Lutchyn, R. M. & Sarma, S. D. Proximity effect at the superconductor–topological insulator interface. *Phys. Rev. B* **81**, 241310 (2010).
46. Guan, S.-Y. et al. Superconducting topological surface states in the noncentrosymmetric bulk superconductor pbtase2. *Sci. Adv.* **2**, e1600894 (2016).
47. Chang, T.-R. et al. Topological Dirac surface states and superconducting pairing correlations in pbtase 2. *Phys. Rev. B* **93**, 245130 (2016).
48. Nadj-Perge, S. et al. Observation of Majorana fermions in ferromagnetic atomic chains on a superconductor. *Science* **346**, 602–607 (2014).
49. Kim, H., Rózsa, L., Schreyer, D., Simon, E. & Wiesendanger, R. Long-range focusing of magnetic bound states in superconducting lanthanum. *Nat. Commun.* **11**, 4573 (2020).
50. Kim, H. et al. Toward tailoring Majorana bound states in artificially constructed magnetic atom chains on elemental superconductors. *Sci. Adv.* **4**, eaar5251 (2018).
51. Schindler, F. et al. Higher-order topological insulators. *Sci. Adv.* **4**, eaat0346 (2018).
52. Benalcazar, W. A., Bernevig, B. A. & Hughes, T. L. Quantized electric multipole insulators. *Science* **357**, 61–66 (2017).
53. Herrera, M. et al. Corner modes of the breathing kagome lattice: origin and robustness. *Phys. Rev. B* **105**, 085411 (2022).
54. Proctor, M., Blanco de Paz, M., Bercioux, D., García-Etxarri, A. & Arroyo Huidobro, P. Higher-order topology in plasmonic kagome lattices. *Appl. Phys. Lett.* **118**, 091105 (2021).
55. Lee, S. et al. Evidence of surface *p*-wave superconductivity and higher-order topology in $MoTe_2$. Preprint at *arXiv* https://doi.org/10.48550/arXiv.2406.07260 (2024).
56. Yao, S. & Wang, Z. Edge states and topological invariants of non-hermitian systems. *Phys. Rev. Lett.* **121**, 086803 (2018).
57. Lubatsch, A. & Frank, R. Behavior of floquet topological quantum states in optically driven semiconductors. *Symmetry* **11**, 1246 (2019).
58. Song, F., Yao, S. & Wang, Z. Non-hermitian skin effect and chiral damping in open quantum systems. *Phys. Rev. Lett.* **123**, 170401 (2019).
59. Dangel, F., Wagner, M., Cartarius, H., Main, J. & Wunner, G. Topological invariants in dissipative extensions of the Su-Schrieffer-Heeger model. *Phys. Rev. A* **98**, 013628 (2018).

Acknowledgements

This work was supported by the National Research Foundation of Korea (NRF), funded by the Ministry of Science and ICT (MSIT), South Korea (Grants Nos. NRF-2022R1A2C1011646, NRF-2022M3H3A1085772, NRF-2022M3H3A1063074, RS-2023-00252085, and RS-2023-00218998). This work was also supported by the Quantum Simulator Development Project for Materials Innovation through the NRF funded by the MSIT, South Korea (Grant No. NRF-2023M3K5A1094813). S.H. Han, M. Kang, and S. Cheon also acknowledge support from the POSCO Science Fellowship of the POSCO TJ Park Foundation.

Author contributions

S.-H.H., M.K., M.J.P, and S.C. conceived and designed the project. S.-H.H. and M.K. performed the tight-binding calculations and analyzed the results under the supervision of M.J.P and S.C. All the authors discussed the results and contributed to the writing of the paper.

Competing interests

The authors declare no competing interests.

Additional information

Supplementary information The online version contains supplementary material available at https://doi.org/10.1038/s42005-024-01737-z.

Correspondence and requests for materials should be addressed to Moon Jip Park or Sangmo Cheon.

Peer review information *Communications Physics* thanks the anonymous reviewers for their contribution to the peer review of this work. A peer review file is available